Nucl. Fusion **53** (2013) 023005 (14pp) doi:10.1088/0029-5515/53/2/023005

Dynamics of the disruption halo current toroidal asymmetry in NSTX

S.P. Gerhardt

Princeton Plasma Physics Laboratory, Princeton, NJ, 08543, USA

Received 21 September 2012, accepted for publication 3 January 2013
Published 28 January 2013
Online at stacks.iop.org/NF/53/023005

Abstract
This paper describes the dynamics of disruption halo current non-axisymmetries in the lower divertor of the National Spherical Torus Experiment (Ono *et al* 2000 *Nucl. Fusion* **40** 557). The halo currents typically have a strongly asymmetric structure where they enter the divertor floor, and this asymmetry has been observed to complete up to eight toroidal revolutions over the duration of the halo current pulse. However, the rotation speed and toroidal extent of the asymmetry can vary significantly during the pulse. The rotation speed, halo current pulse duration, and total number of revolutions tend to be smaller in cases with large halo currents. The halo current pattern is observed to become toroidally symmetric at the end of the halo current pulse. It is proposed that this symmeterization is due to the loss of most or all of the closed field line geometry in the final phase of the vertical displacement event.

(Some figures may appear in colour only in the online journal)

1. Introduction

Tokamak plasmas are prone to events known as disruptions [1, 2] where an extremely rapid breakdown of plasma confinement, known as the thermal quench [1, 2] leads to a sudden decay of the plasma current in the then cold plasma [3–8]; this latter phase is called the current quench. The thermal loading during the thermal quench [1, 2, 9–13] can lead to severe melting or ablation of the plasma-facing components (PFCs), while the eddy currents driven by the current quench can lead to large forces on in-vessel structures [11]. Finally, it is possible for a large fraction of the plasma current to be converted to a runaway electron beam [1, 2, 14–23], potentially leading to severe localized damage to in-vessel components if position control of the beam is not maintained [24].

Beyond these three effects, there is a fourth damaging phenomenon during a disruption. The control of the plasma vertical position is often lost during a disruption, resulting in a 'vertical displacement event', or VDE. The VDE results in the plasma coming into contact with the PFCs at the top or bottom of the confinement chamber. Currents have been observed to flow from the plasma into the PFCs, through the various in-vessel structures, and then out of a different set of PFCs back into the plasma. These currents, which have historically been known as 'halo currents', have been observed in the conventional aspect ratio tokamaks DIII-D [3, 25–28], JET [29–34], ASDEX-Upgrade [35, 36], COMPASS-D [37], JT-60 [38] and ALCATOR C-MOD [39], and in the spherical torii MAST [40] and NSTX [41]. When the current path in these in-vessel components crosses the strong tokamak magnetic field, the resulting $J \times B$ forces can result in severe damage.

The dynamics of these halo currents can be quite complex. For instance, they need not be axisymmetric; toroidal peaking factors of these currents, defined as the maximum detected halo current normalized by the mean halo current for a toroidal distributed array of sensors, have been observed with values exceeding 4 in conventional aspect ratio tokamaks [2]. Hence, the forces can be concentrated on a subset of the tokamak components. Furthermore, the halo current asymmetries have been observed to rotate toroidally [34, 39]. If the rotation frequencies are a match to the resonant frequencies of the various in-vessel components, then the potential for damage is further increased [34]. As a consequence of their damaging potential, the details of these non-axisymmetric halo currents have been the subject of numerous recent theoretical studies [42–46], largely developing the idea that the non-axisymmetric halo currents are surface currents that develop to stabilize the otherwise Alfvénic growth of the external kink mode.

This paper expands on the NSTX halo current data presented in [41], by focusing on spatial and temporal dynamics of the currents where they enter the divertor floor. Section 2 describes the NSTX device and halo current measurements. Section 3 describes the observations of halo current rotation, using examples from a number of discharges. Section 4 examines some statistics of the halo current rotation, while section 5 examines the impact of large $n = 1$ applied fields on the rotational dynamics. Section 6 proposes an explanation for the observed halo current symmeterization late in the halo current pulse. A summary and discussion are provided in section 7.

Finally, it is worth noting that various terminologies have been used recently for these currents. Historically, they have been referred to as 'halo currents', or possibly 'disruption

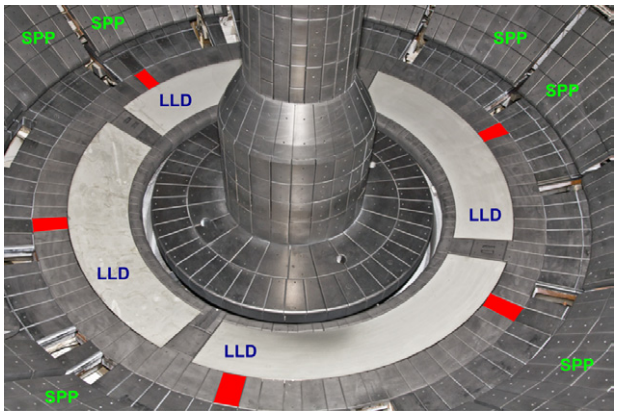

Figure 1. Location (in red) of the row-3 shunt tile diagnostics used for the measurements in this paper. A sixth tile is located behind the centre column. For reference, both the liquid lithium divertor (LLD) and secondary passive plates (SPPs) are labelled.

halo currents'. Recent work by Zakharov [43] has introduced the phrases 'Evans currents' and 'Hiro currents', denoting different mechanisms that can drive these currents. From a purely experimental perspective, it appears that a phrase such as 'disruption scrape-off layer currents' would be most accurate. However, in this paper, the phrase 'halo currents' will be used in order to be consistent with previous experimental usage, and without any judgment about the underlying physics.

2. NSTX device and halo current instrumentation

NSTX [47] is a medium scale spherical torus located at Princeton Plasma Physics Laboratory. The typical major radius of the plasma is 0.85 m, with typical aspect ratios of $1.35 < A < 1.55$. Typical plasma currents are in the range $500 < I_P(\text{kA}) < 1300$, with toroidal fields in the range $0.35 < B_T(\text{T}) < 0.55$. Neutral beam heating [48] powers are typically up to 7 MW, with high-harmonic fast wave (HHFW) power [49] up to ~6 MW at 30 MHz.

As described in [50], NSTX has been outfitted with a diverse array of halo current diagnostics. The data from these various diagnostics was described in great detail in [41]. This paper focuses on a detailed analysis of a small subset of that data, namely, the data collected by the lower outer divertor 'shunt tiles'.

The locations of these tiles are indicated in the photograph in figure 1; also indicated in the figure are the liquid lithium divertor (LLD) [51] trays, and the secondary passive plates (SPPs). These shunt tiles are fitted with compact resistive shunts where they are fastened to the divertor floor; the voltage on these shunts is used to infer the current flowing into the tile. This shunt tile data was digitized at both 5 and 500 kHz. Only the faster sampled data is used in this paper. The local current densities are calculated as the current collected by each tile normalized by the area of the face of each tile. The set of shunt tiles in figure 1 was only available during the 2010 run campaign. Hence, all data illustrated in this paper come from that run period.

For reference, the plasma current direction was counter-clockwise when viewed from above, or into the plane of figures 2(*b*) and 5(*b*). The toroidal field (TF) rod current was downwards, leading to a TF in the clockwise direction when viewed from above. The NSTX neutral beams, used in all discharges described in detail in sections 3, 5, and 6 and most discharges in the database analysis in section 4, are oriented in the co-injection direction, i.e. injection parallel to the plasma current.

3. Observation of halo current rotation in the NSTX divertor

As stated in the introduction, there have been numerous instances where many toroidal revolutions of the halo current pattern occur during the disruption. An example of this discharge variety is in figure 2. Figure 2(*a*) shows the plasma current evolution and figure 2(*b*) shows the reconstruct plasma boundary for time slices immediately before the phase with large halo currents. The colours of the boundary reconstructions correspond to the times of the vertical lines in the plasma current trace. It is clear that this case is a downward VDE, with the point of contact on the inner half of the lower outer divertor.

The contours of the halo current as a function of toroidal angle and time are shown in figure 2(*c*); the colours are arbitrarily scaled so that the darkest blue corresponds to the maximum current out of the tiles for this particular case. Some small amount of current begins to flow just after $t = 0.407$ s. This current is largely localized to three adjacent tiles (from a total of six) and flows for ~3 ms at this toroidal angle. Throughout this phase of small halo current, the edge safety factor (q_1) is constantly decreasing as the plasma moves down and the cross-section shrinks at approximately constant I_P. As q_1 decreases to 2 at about $t = 0.41$ s in figure 2(*e*), two significant changes in the nature of the currents can be observed. First, there is a gradual increase in the halo current magnitude. Second, the non-axisymmetric component of the halo current pattern begins to rotate. In this particular case, approximately four complete toroidal circuits of the divertor are made by the asymmetry. The direction of rotation is opposite that of the plasma current, and opposite to that induced by the co-injected neutral beams.

This rotation is emphasized in figure 2(*c*) by the black, green and magenta lines tracing out the contours; these curves are determined as follows. At each time slice, the toroidal variation of the halo current is fit to a form:

$$J_{HC}(\phi) = J_{HC,n=0} + J_{HC,n=1}\cos(\phi - \phi_{n=1}). \qquad (1)$$

Here, $J_{HC,n=0}$, $J_{HC,n=1}$ and $\phi_{n=1}$ are fit parameters. Of course, the actual toroidal distribution may be significantly more peaked than a simple cosine; this fit is simply used to track the phase and approximate asymmetry magnitude. More complex fits, which allow the toroidal extent of the halo current to be properly tracked, will be discussed later in this section. The black, green and magenta line in figure 2(*c*) is then the time-dependent phase $\phi_{n=1}$ determined by this fitting procedure using equation (1).

The colours are indicative of various times in the halo current pulse, as indicated schematically by figure 3(*a*). The $n = 1$ component of a *model* halo current pulse is shown in that figure. The duration where the current is greater than

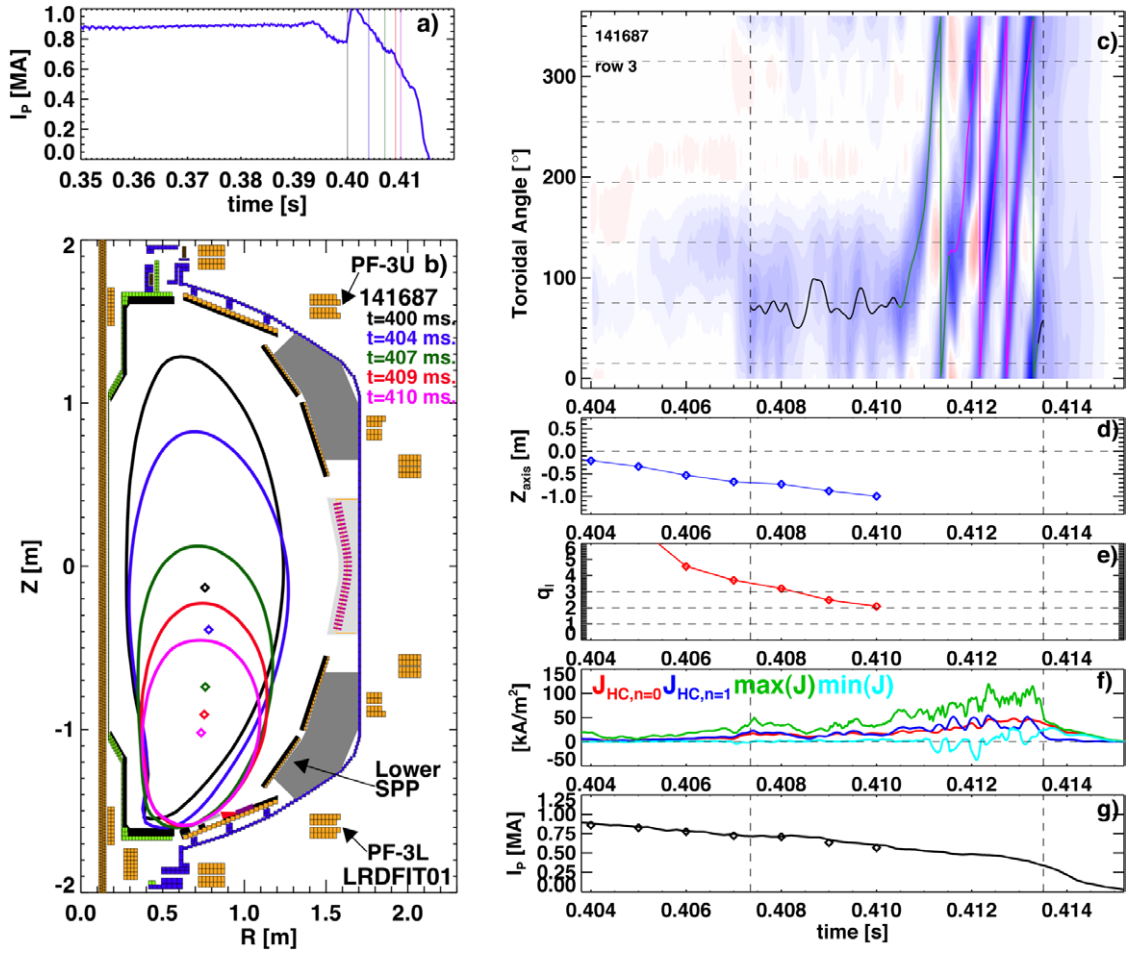

Figure 2. Dynamics of a discharge that shows significant halo current rotation. Shown are (*a*) the plasma current and (*b*) plasma motion leading up to the large halo current phase, (*c*) the contours of halo currents in the lower divertor row #3 versus time and toroidal angle, (*d*) the magnetic axis position, (*e*) the edge safety factor, and (*f*) the $n = 0$ and $n = 1$ components of the halo current, as well as the maximum and minimum values of the halo current on any single tile, and (*g*) the plasma current again.

75% of the maximum is indicated in magenta, greater than 50% in green, and greater than 25% in black. These various time windows are well defined for any given pulse shape. In the analysis below, quantities will be averaged over these windows. Note that in reality, the current may rise above one of these threshold levels, fall beneath it, then rise above it again. However, to avoid complications, the windows are defined by the first time the current exceeds the stated fraction, and the last time it drops beneath that fraction.

Figures 2(*f*) and (*g*) show additional details of the halo and plasma current evolution. The $n = 0$ and $n = 1$ components of the halo current, determined from fits to equation (1), are indicated in red and blue respectively. These components have similar magnitude through the majority of the pulse. This observation, along with the contours in figure 2(*c*), indicate that the fundamental structure of the current entering the divertor floor is a toroidally localized lobe. The approximately equal $n = 0$ and $n = 1$ components are present because, at any given poloidal location, the halo currents tend to have only a single sign; it is rare for current to both flow into some tiles and out of others at the same poloidal location.

This last statement is made clear by the traces of the minimum and maximum halo current flowing in any of the six tiles, also shown in figure 2(*f*). The maximum value tends to be approximately equal to the sum of the $n = 0$ and $n = 1$ parts, while, except for brief transients, the minimum value hovers around zero. Note that the similar contour plot from AUG, figure 15 of [36], shows a similar large lobe structure.

The primary exception to the observation of strong asymmetries can be found after $t = 0.4135$ in figures 2(*c*) and (*f*). After this time, the non-axisymmetric component of the halo current decays rapidly, leaving behind a largely axisymmetric residual current; the values of $\min(J)$, $\max(J)$ and $J_{\mathrm{HC},n=0}$ overlap during this phase. This residual $n = 0$ current decays at a rate comparable to the plasma current. As will be shown in section 6, it appears that this corresponds to the phase when the magnetic axis has been nearly or completely driven into the divertor floor, and open-field line currents dominate.

More details of the halo current asymmetry dynamics for this discharge can be observed in figure 4. In this figure, a more sophisticated fitting function for the toroidal dependence is used, given by equation (2):

$$J(\phi, t) = f_0 + f_1 \frac{(1 + \cos(\phi - f_2 - f_3 t))^{f_4}}{2^{f_4}}. \qquad (2)$$

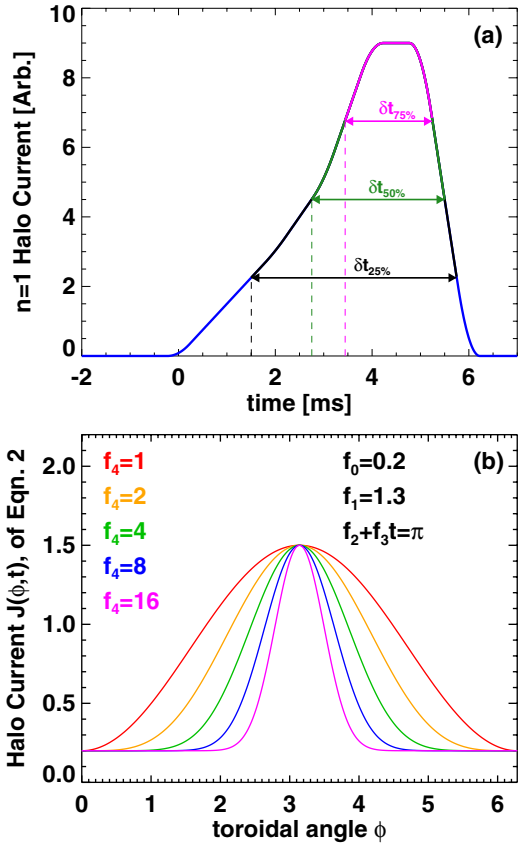

Figure 3. (*a*) Definition of the 25%, 50% and 75% levels for halo current pulse analysis, and (*b*) model curves showing the toroidal dependence of the fitting function equation (2). See text for further details.

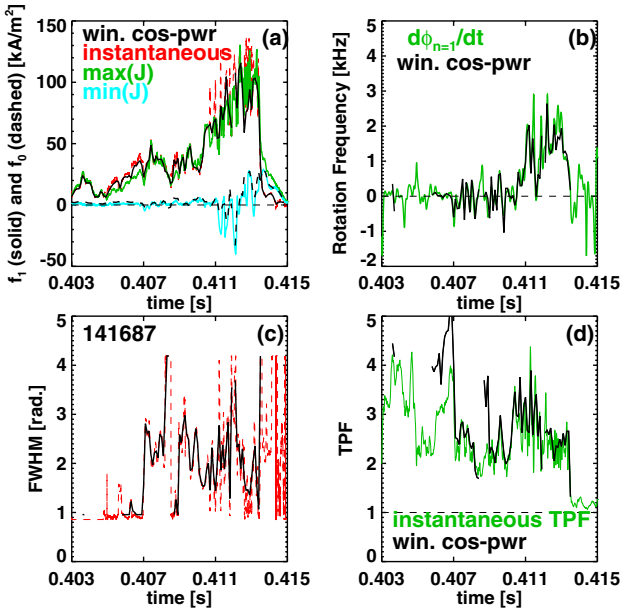

Figure 4. Details of the toroidal asymmetry evolution for the discharge in figure 2. Shown are (*a*) the axisymmetric and non-axisymmetric amplitude components, as well as the maximum and minimum current on any individual tile, (*b*) the toroidal rotation frequency of the perturbation determined by two different methods, the (*c*) FWHM and (*d*) toroidal peaking factor of the halo currents. The red curves in (*a*) and (*c*) come from fits of equation (2) at each time slide individually, with the f_3 term eliminated. The phrase 'win. cos-pwr' refers to the windowed cosine-power fits of equation (2). See text for further details.

Example curves of this function are shown in figure 3(*b*). f_0 represents the toroidally uniform current amplitude, while f_1 represents the amplitude of any toroidal peaking. The parameter f_3 is the rotation frequency, that, along with offset phase f_2, determine the instantaneous toroidal phase of the asymmetry; the example curves in figure 3(*b*) have $f_2 + f_3 t = \pi$, in order to centre the waveform in the plot window. The parameter f_4 controls the width of the peak in the toroidal angle. This parameter is scanned from 1 to 16 in the example in figure 3(*b*), showing how this fit function can represent toroidally localized halo currents.

To apply this fit, the data is broken into small time windows of duration δt, and the $6\delta t/\tau_s$ data points in each window are used to constrain the fit; here, the 6 refers to the number of shunt tiles and τ_s is the sampling interval. A non-linear fitting routine (lmfit, from [52]) is used to fit the parameters of equation (2) during this time window; note that it is only by fitting within a time window long enough for some halo current rotation to occur that the parameter f_3 can be determined. Hence, each of the parameters f_0 through f_4 determined by the fits corresponds to the average value over the small time windows. δt of 0.1 ms has been used for the calculations in this paper.

Four features of this fit function and fitting method are worth noting. First, if a fit function does not include some time dependence, but rather only toroidal angle dependence, then it can less accurately model highly peaked functions, which may only instantaneously manifest themselves on a single tile. However, if the feature is rotating, then the motion of the features across the tiles can be captured in the time dependence of equation (2). Of course, if the feature is both toroidally peaked and nearly stationary, then it can be difficult to assess even with equation (2). Secondly, the toroidal rotation velocity is a direct parameter in the fit, allowing it to be calculated without the noise-inducing differentiation of the asymmetry phase ($\phi_{n=1}$) versus time. Third, the fit function only works well when there is a single toroidal lobe; less common cases with $n = 2$ (or higher) variation cannot be fit. Finally, it should be noted that an alternative means of writing the function in equation (2) is

$$J(\phi, t) = f_0 + f_1 \cos^{2f_4}\left(\frac{\phi - f_2 - f_3 t}{2}\right).$$

The results of such a fit are shown in figure 4, for the same discharge (141687) as in figure 2. Figure 4(*a*) shows the parameters f_0 and f_1 as black dashed and solid lines respectively. A related version of the parameter f_1, derived from fitting the toroidal dependence at each individual time slice using a version of equation (2) with no parameter f_3, is shown with a red dashed line. A comparison of these two values of f_1 shows that fitting during windows with an explicit time dependence (solid black) produces a more smooth amplitude than fitting at each time point individually (red dashed). The non-axisymmetric part of the current (f_1) is completely dominant, with the parameter f_0 oscillating around zero for most of the disruption. It is only at the end of the halo current pulse, during the symmeterization phase, that the parameter f_0 becomes large compared to f_1.

The green trace in figure 4(*a*) shows the maximum current detected on any single shunt tile at each time, while the cyan trace shows the minimum current on any tile. This metric is motivated by the observation that for $f_0 = 0$, the parameter f_1 is exactly equal to the maximum current. As expected, the green trace overlaps the value of f_1, except for during those brief periods where f_0 and the minimum local current are non-zero.

The average rotation frequency of the perturbation is shown in figure 4(*b*). The frequency $f_3/2\pi$, as determined by the fits of equation (2) within the time windows, is shown in black. The frequency in green results from differentiating the time-dependent toroidal phase $\phi_{n=1}$ from the fits of equation (1). Good agreement is found between the two methods. During the phase $0.406 < t < 0.410$, both calculations show the frequency oscillating about 0 kHz. Starting at $t = 0.410$, the asymmetry begins to rotate, with frequencies of typically 1.5–2.0 kHz. However, there is a brief pause in the rotation in this phase of high rotation at $t = 0.4115$ s, visible somewhat subtly in figure 2(*c*) and clearly in figure 4(*b*).

Figures 4(*c*) and (*d*) show additional dynamics of the toroidal asymmetry. The full-width at half-maximum (FWHM) of the fit toroidal distribution is shown in figure 4(*c*). Values from both the windowed time-dependent fits (black) and the instantaneous fits (red dashed) are shown, and the benefits of using the full equation (2) with an explicit frequency term in reducing variations in the fit parameters are clear. Early in the halo current pulse, the toroidal width is typically ∼2 rad. During the high rotation phase starting at $t = 0.41$, the width varies from ∼1.5 rad up to 3 rad, and then back towards 1.4 rad again. Note that the simple $n = 1$ toroidal dependence $I_{HC} \sim f_0 + f_1 \cos(\phi)$ has a FWHM of π radians, which is generally significantly larger than that observed in figure 4(*c*). The toroidal peaking factor in figure 4(*d*) is calculated both using the raw data at each time slice (blue), and using the fit equation (2). The two methods generally agree well, and show significant variation in time.

As described in detail in [41], VDEs with the trajectory in figure 2, where the plasma lands on the outboard divertor floor, are the most common in NSTX. However, it is also reasonably common to find examples where the VDE lands on the SPPs. While most of the halo field lines strike the passive plates in these examples, some also land on the outboard divertor, where halo currents are measured. An example of such a case is shown in figure 5.

Figure 5(*a*) shows that the initially centred plasma first drifts upwards following a β collapse at $t = 0.42$. The vertical position control system attempts to counteract this motion, and in doing so actively drives the plasma into the lower SPP. The vertical motion leading up to the final disruption is shown in figure 5(*d*), when it is clear that the plasma moves very rapidly downwards at $t \sim 0.477$ s. Interestingly, the edge safety factor in figure 5(*e*) actually increases for a phase, as the plasma cross section increases as it moves off the upper divertor. However, the edge q then drops rapidly when the plasma strikes the lower SPPs.

The contours of halo current density are shown in figure 5(*c*). Once again, it is clear that there is (i) a significant toroidal asymmetry in the outboard divertor halo current pattern, and (ii) significant rotation of the asymmetry, again in the direction opposite the plasma current. In this case, the pattern completes almost 1.5 toroidal transits during the halo current pulse. However, the magnitude is far more irregular in time compared to the example in figure 2, potentially due to the location of these sensors farther from the VDE limiting point.

Figure 5(*f*) shows that the $n = 1$ and $n = 0$ components of the halo current again have comparable magnitude; the signs are different in this case, since the current is, on average, flowing into the divertor floor in this case, instead of out as in figure 2. In this case, the maximum halo current hovers around zero, while the minimum current is in magnitude comparable the sums of the $n = 0$ and 1 parts. This reinforces the observation of the dominant structure being a toroidally localized lobe. Also as before, the halo current asymmetry decays at the end of the pulse, leaving a brief period of dominant $n = 0$ halo current. This phase of the discharge will be discussed again in section 6.

Figure 6 shows four additional examples of these dynamics for disruptions that limit on the outboard divertor floor, as in figure 2. In each case, the halo current contours are shown in the large frame, with the $n = 0$ and 1 decompositions, the minimum and maximum currents at any individual tile, and the plasma current waveforms in the lower frames.

Figures 6(*a*) through (*f*) illustrate examples with large currents, but minimal rotation; these two discharges have the largest halo current magnitudes observed by the row-3 shunt tiles in NSTX during the 2010 run campaign. Note that there is almost no discernable toroidal rotation in figure 6(*a*), and less than a full revolution in frame (*d*) during the phase of large halo currents. Also note that the contours in figure 6(*a*) cannot always be described with a single lobe. For instance, at $t = 0.45$ s, current is observed in the tiles at 15° and 75°, as well as at 195°, but with little current on the tiles between. Hence, the fits using equation (2) would not produce meaningful results for this phase of the halo current pulse.

Figures 6(*g*) through (*i*) show an example where, as in figure 2, substantial rotation of the halo current pattern is observed. In this case, the initial low-level currents starting at $t \sim 0.423$ are already rotating. The rotation appears to stagnate twice, at $t = 0.427$ and $t = 0.4285$, before beginning a phase of rapid rotation. In this case, seven total revolutions of the halo current pattern are observed.

Figures 6(*j*) through (*l*) show an example where the halo current rotation behaves in an apparently erratic manner. A low level of current begins to flow at $t = 0.503$, and unlike the case in figure 2 but like that in figure 6(*g*), has clear toroidal rotation. There is a period of stagnation at $t = 0.506$, but the rotation is then resumed. However, at $t = 0.508$ s, the rotation actually changes sign, rotating slowly in the co-I_P direction. This lasts until $t = 0.51$, after which the pattern makes two rapid rotations in the counter-I_P direction.

In all cases in figure 6, the $n = 0$ and $n = 1$ halo current magnitudes are comparable through the duration of the pulse. The minimum halo current measured on any tile typically hovers around zero, except for small transients. Finally, all of the examples in figure 6 show a late symmeterization of the halo current pulse. This is most clear in the example in figures 6(*g*) and (*h*), but can be found to a lesser extent in all other cases.

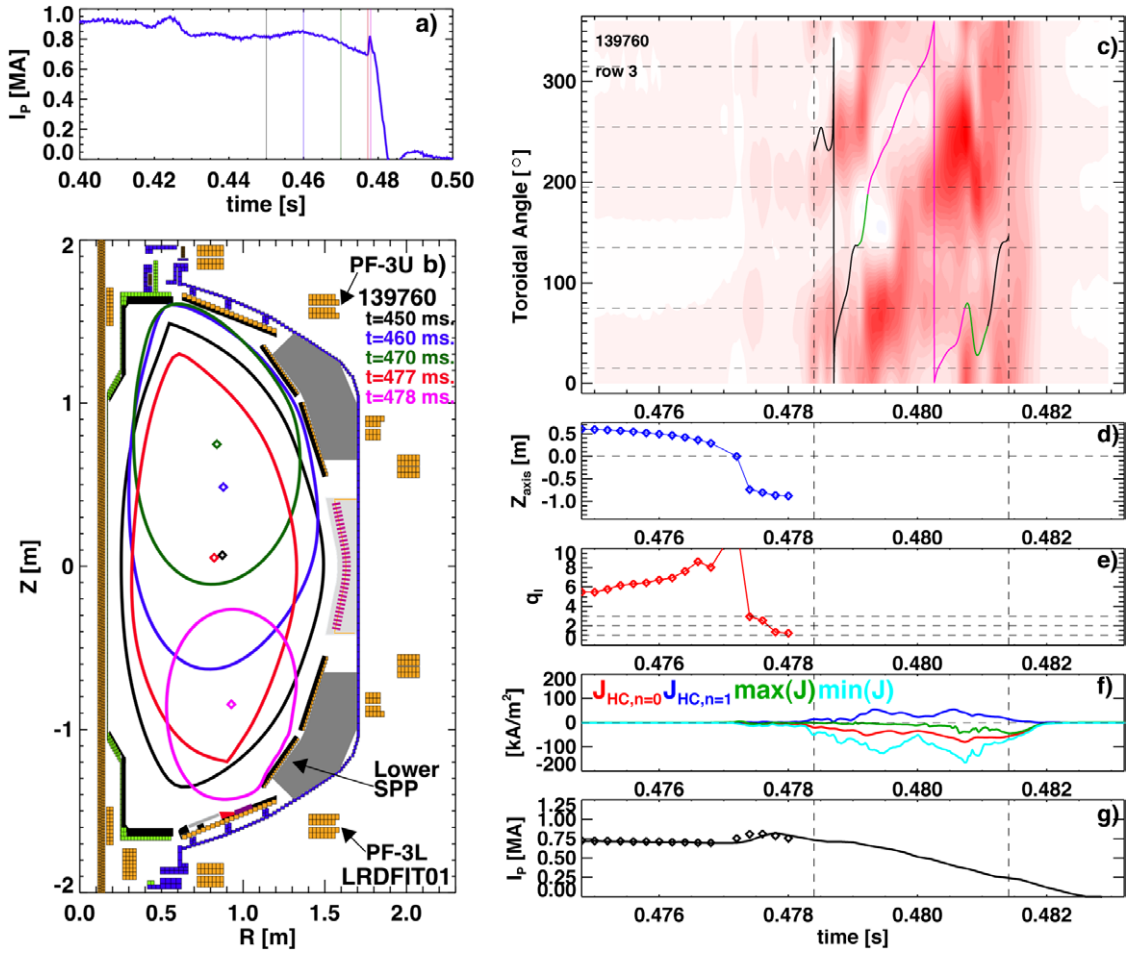

Figure 5. Example of halo current dynamics for a case where the plasma limits on the lower secondary passive plates (SPP). The individual frames show the same quantities as in figure 2. Figure (*c*) shows that ∼1.75 revolutions of the halo current asymmetry occur in this case.

The dynamics of the 'erratic' discharge, 139369 in figures 6(*j*)–(*l*), are illustrated in greater detail in figure 7; the analysis techniques here are the same as described in relation to figure 4. The baseline (f_0) and toroidally localized (f_1) components of the current are shown in figure 7(*a*), along with the minimum and maximum currents. It is clear again that the purely axisymmetric part is rather small in magnitude during most of the halo current pulse. The maximum instantaneous current is again comparable to the value of f_1.

The rotation frequencies are shown in figure 7(*b*), where both the fits during time windows (black) and the differentiation of the $n = 1$ phase (blue) are shown. This figure illustrates a phase between 0.502 and 0.5058 s during which the rotation is fairly uniform. There is then a short phase of rotation in the co-I_P direction, at $t = 0.506$. The rotation then returns to the counter-I_P direction for ∼2 ms, with rotation frequencies of ∼1 kHz. This is followed by a second stagnation and reversal of the rotation between $t = 0.508$ and 0.510. Finally, a burst of rotation at $t = 0.510$ results in the final two toroidal revolutions.

The FWHM in figure 7(*c*) and the peaking factor in figure 7(*d*) also show quite complicated temporal dynamics. The FWHM shows periods where the lobe is quite narrow (FWHM $\lesssim$2 rad), and cases where it is quite broad; interestingly, the periods with a broad lobe at $t = 0.506$ and $t = 0.509$ correspond to the two stagnations in the rotation velocity. The TPF also varies rapidly, with a mean of ∼2 through most of the halo current pulse.

To summarize this section, the examination of individual discharges demonstrates that the dynamics of halo currents can be quite complicated. Essentially all cases have a significant toroidal asymmetry; indeed, the dominant structure is typically a large lobe of current, whose toroidal localization may be significantly more severe than a simple $n = 1$ cosine dependence. This asymmetry is often observed to rotate toroidally, though the frequency can vary substantially during the relatively short period with large halo currents. The characteristic width of the asymmetry and associated peaking factor can also vary rapidly during a single discharge.

4. Statistical analysis halo current dynamics

In order to establish the relative occurrence levels for these various events, a database of the 732 discharges with the largest halo currents observed by the row-3 tiles has been formed. The typical rotation speed, number of rotations, and pulse durations were established, averaged over the periods when the $n = 1$ halo current is greater than 25%, 50% and 75% of its maximum in that pulse (the 25%, 50% and 75% basis in the plot captions, and see the description of figure 3(*a*) for further discussion of

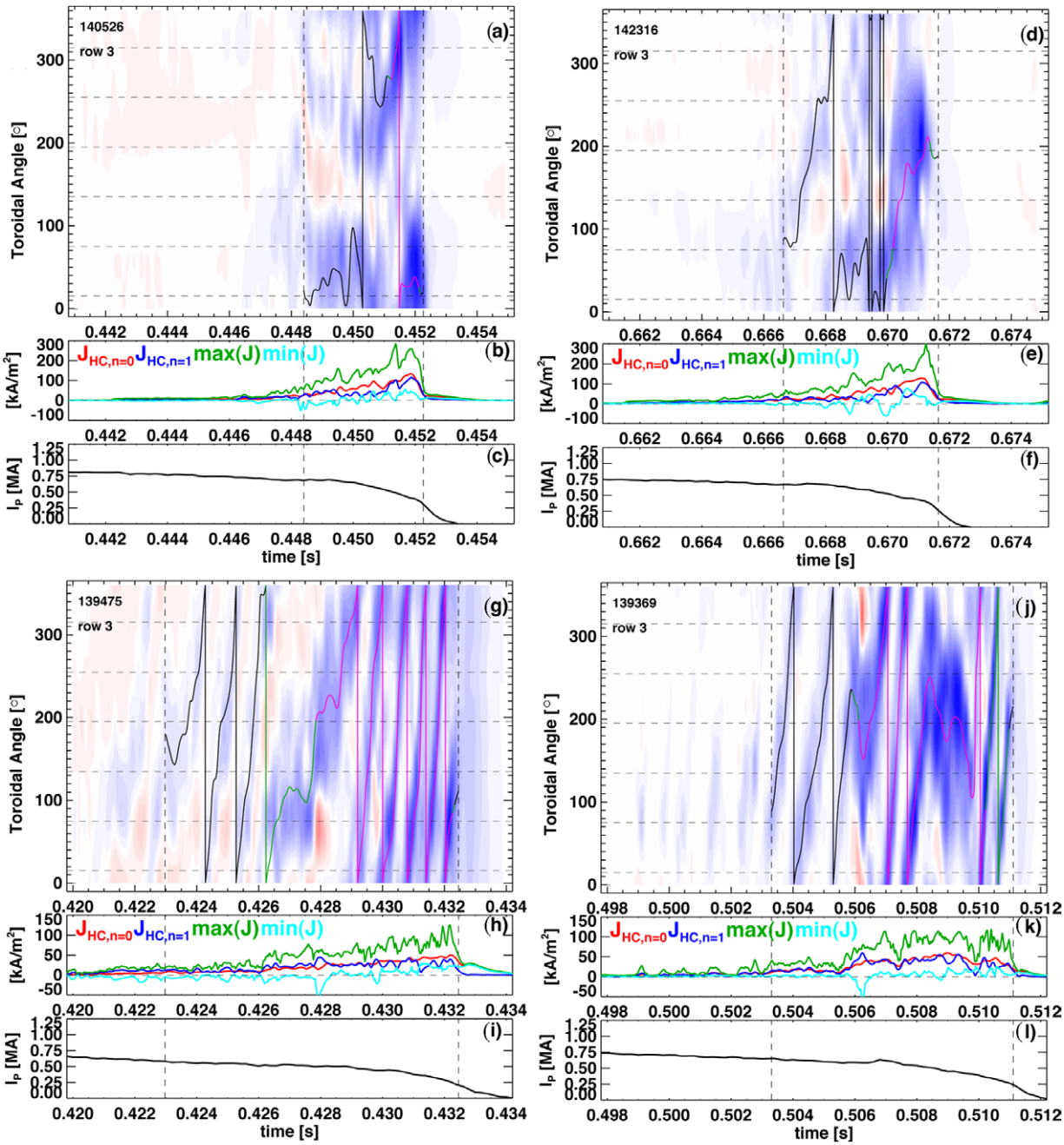

Figure 6. Four additional examples of the halo current asymmetry evolution. The time window is 14 ms long for each case. See text for further details.

these time windows). Note here that because the shape of the $n = 0, n = 1$, and $\max(J)$ (or $\min(J)$) curves are so similar on figures 2, 5 and 6, the time windows would not be meaningfully different if a criterion other than the $n = 1$ amplitude were used in determining the averaging windows. Also included in the database are the various equilibrium properties of the plasma before the disruption and information about any magnetic braking applied to the plasma.

A set of results from these studies is shown in figure 8, where the colours indicate the averaging window as per figure 3. A histogram of rotation frequencies is shown in figure 8(*a*). For any of the 25%, 50% or 75% basis, the most typical rotation frequencies are $\lesssim$700 Hz in NSTX. However, for the higher percentage basis calculations, which are localized to a smaller time during the halo current pulse, rotation frequencies of up to 2 kHz have been observed.

The durations of the various periods are shown in figure 8(*b*). For the 75% basis, corresponding to the period of peak halo current, the durations are most commonly 0.5–2.5 ms, but with a tail out to ~6 ms. For the 25% basis, encompassing the majority of the halo current pulse, the durations are typically ~3 to ~7 ms long.

Figure 8(*c*) shows the total number of rotations. For the 25% basis, there are examples with up to 8 toroidal revolutions. For the 50% basis, that number is reduced to 5, while it drops to ~4 for the 75% basis. Note that the numbers in these figures

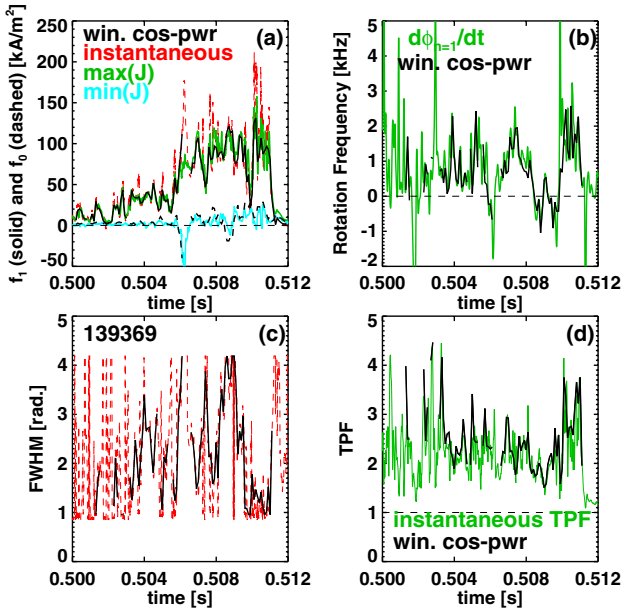

Figure 7. Details of the toroidal asymmetry dynamics for the discharge in figures 6(*j*) through (*l*), which shows rather erratic behaviour of the halo current rotation. The quantities plotted are the same as in figure 4.

are consistent, in that, taking the 25% basis as an example, typical durations of 5 ms and rotation frequencies of 300 Hz imply that ∼1.5 revolutions should be common, as found in figure 8(*c*).

A key question is whether these rotation dynamics are strongest in cases with larger or smaller halo currents. This is answered in figure 9, where scatter plots of the rotation frequency, pulse duration, and total number of revolutions are shown as a function of two measures of the halo current magnitude. The first measure is the simple $n = 0$ current magnitude, calculated as the average of the current in the six tiles at each time step. The second metric is the instantaneous maximum of the six halo current signals, motivated by the discussions in section 3. In both cases, the plotted current is averaged over the time when the $n = 1$ magnitude is greater than 50% of the peak.

Figures 9(*a*) and (*b*) show the rotation frequency of the asymmetry, determined on the 25%, 50% and 75% basis, as a function of the $n = 0$ and maximum halo current. In both cases, there is a strong trend for the envelope of the rotation frequency to be rather small when the halo current amplitudes are strongest, and for the largest halo current rotation frequencies to occur in cases with smaller halo currents. The pulse durations are shown in figures 9(*c*) and (*d*). Once again, the envelope of data shows a trend of longer pulse durations when the halo current magnitude is smaller, and shorter durations when the magnitude is larger.

The net result of these trends is shown in figures 9(*e*) and (*f*). The envelope of the total number of rotations tends to be a strong function of the total halo current magnitude. Cases with large halo currents tend to have a small number of rotations, while those with smaller halo currents often, but not always, have larger numbers of rotations. This statement is true whether the halo current magnitude is measured by the

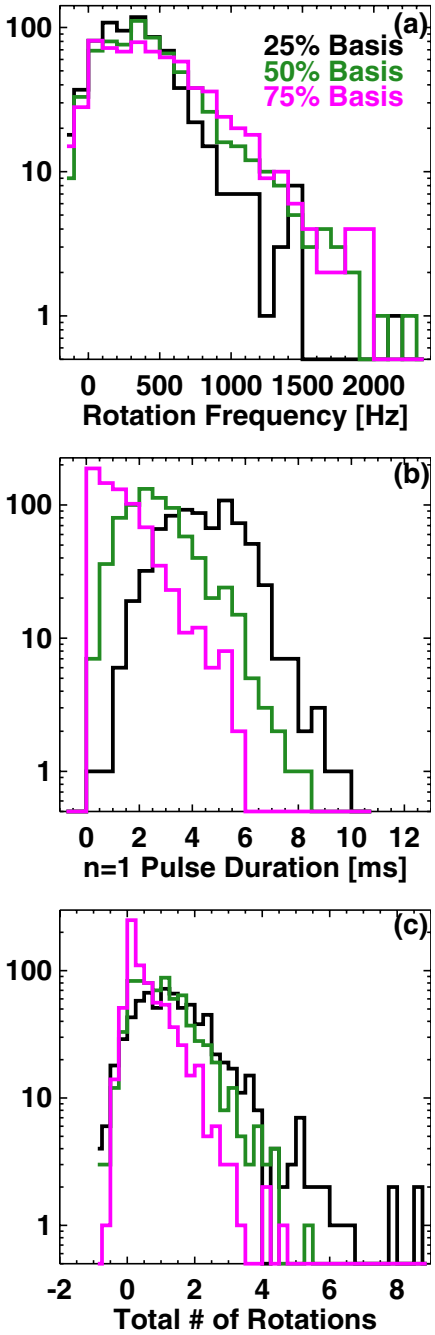

Figure 8. Histograms of (*a*) the rotation frequency, (*b*) the pulse duration, and (*c*) the total number of revolutions, for a database of 732 discharges. The colour code corresponds to different phases of the halo current pulse, as described in figure 3, and all cases are downward VDEs roughly similar to that in figure 2. Note the logarithmic scale on the *y*-axis.

toroidally average component or by the maximum local halo current.

The absolute magnitude of the halo currents, measured in amperes, will of course vary from device to device. The most common normalization of the halo current magnitude is the plasma current itself, here denoted $I_{P,D}$ and measured just before the initiation of the final current quench [5, 6]; this is called the halo current fraction (HCF). Here, the total halo current is estimated by taking the average current measured by

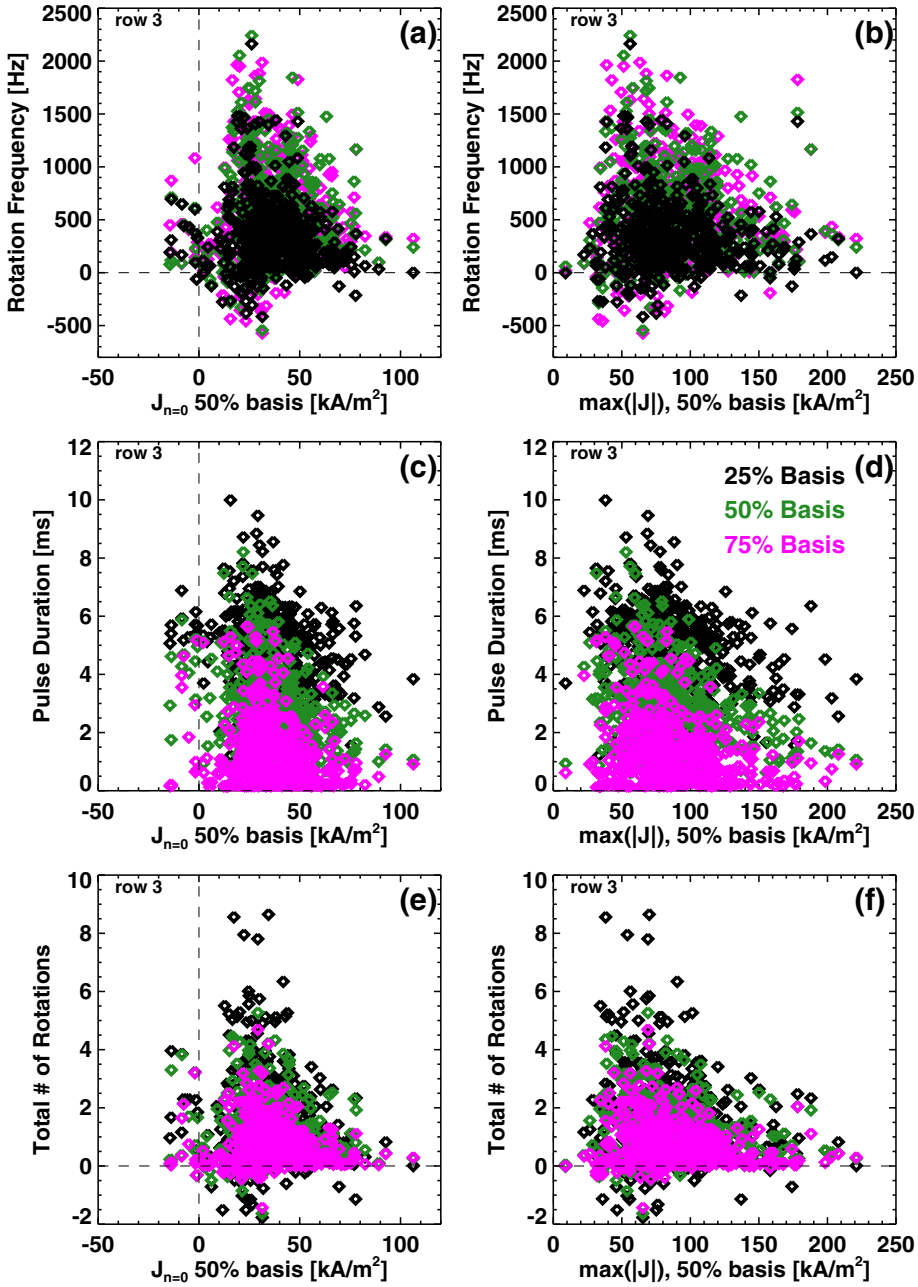

Figure 9. Plots of the rotation frequency in (*a*) and (*b*), pulse duration in (*c*) and (*d*), and total number of revolutions in (*e*) and (*f*). The left column shows that data plotted against the $n = 0$ halo current magnitude averaged over the 50% time window, while the right column shows the data plotted against the maximum measured current density, averaged over the 50% time window.

the six tiles at each time and multiplying it by the ratio of the area of all tiles in row 3 of the outboard divertor to the area of the six measuring tiles. The halo current fraction so defined is then averaged over the period where the $n = 1$ halo current is greater than 50% of its maximum value.

The results of such analysis are shown in figure 10. Frame (*a*) shows the bounding envelope of the rotation frequency generally decreasing with halo current fraction, though there are some clear outliers at large halo current fraction and large rotation frequency. Figure 10(*b*) shows that the envelope on the pulse duration drops rapidly as the halo current fraction increases. This emphasizes that cases with large halo currents tend to have them for only a short amount of time. The result of these two observations is that the envelope of the total number of rotations tends to decrease rapidly as the halo current fraction is increased. This is a positive result for future tokamak/ST facilities, as it implies that the largest resonant amplification factors may not be applied to the largest halo loads. However, confirmation of this trend on other devices is clearly required before it can be extrapolated to ITER.

5. Effect of $n = 1$ fields on halo current rotation

The impact of large $n = 1$ field on the rotation dynamics has also been studied. This has been done by (i) examining a large database of NSTX discharges and (ii) applying $n = 1$ fields

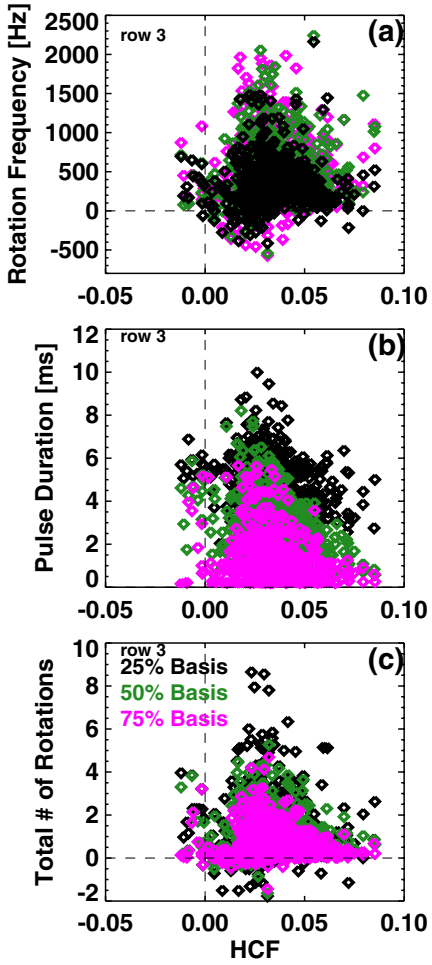

Figure 10. Plots of the rotation frequency in (*a*), pulse duration in (*b*), and total number of revolutions in (*c*), as a function of the halo current fraction (HCF). The HCF is averaged over the period when the $n = 1$ halo current is greater than 50% of its maximum value. See text for additional details.

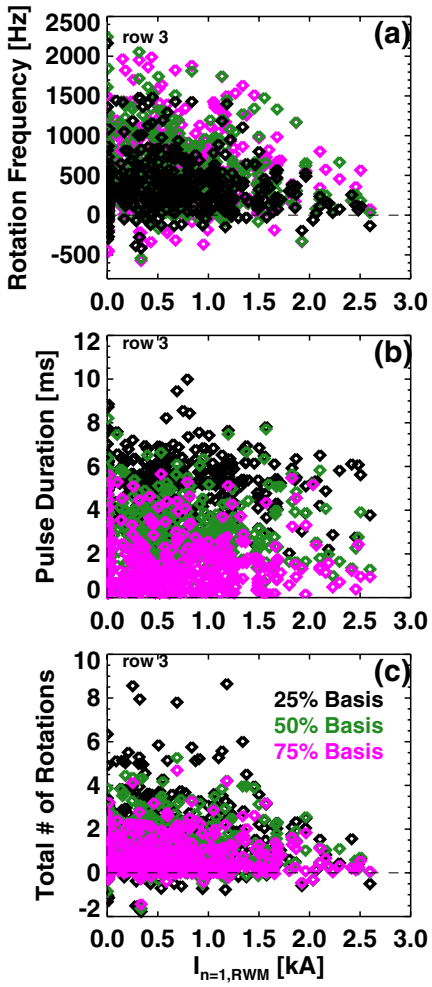

Figure 11. Plots of the rotation frequency in (*a*), pulse duration in (*b*), and total number of revolutions in (*c*), as a function of the $n = 1$ applied field.

to deliberate VDEs. Those two studies will be discussed in that order in this section. These studies are motivated by the observation that $n = 1$ fields can brake the plasma rotation, by applying either a localized $J \times B$ torque at the integer q surfaces [53], or a more radially distributed torque from neoclassical toroidal viscosity (NTV) [54–56].

NSTX has an array of six midplane radial field coils [57], which are used for magnetic braking [56, 58, 59], dynamic $n = 1$ error field correction [60], pre-programmed $n = 3$ error field correction [61], and fast $n = 1$ RWM control [59, 62]. It is common for the final-mentioned use of the system to apply large $n = 1$ fields during the disruption, both due to the actual 3D distortions of the plasma and inaccuracies in reconstructing the magnetic perturbation amplitudes during rapid disruption dynamics. As a consequence, many different levels of applied $n = 1$ fields were present during the disruptions studied in this paper.

Figure 11(*a*) shows the typical rotation frequencies as a function of the $n = 1$ applied field amplitude, as measured by the coil currents; the maximum allowed power supply current is 3.2 kA. It is immediately clear that the envelope of rotation frequency, measured on any of the 25%, 50% or 75% basis, is reduced for large values of the $n = 1$ applied field. The pulse duration in figure 11(*b*), however, is largely independent of the applied field magnitude. The net result, shown in figure 1(*c*), is that envelope on the total number of revolutions is reduced when the $n = 1$ applied field magnitude is large. Of course, the number of samples at higher currents is relatively small, and so the statistical uncertainty in this conclusion may be large.

The coil current magnitudes are an NSTX-specific quantity. To put them in perspective, the $n = 1$ B_R perturbation at the midplane has been computed, on a circle with radius $R = 1.45$ m (approximately the outboard midplane radius for H-mode plasmas). Note that this calculation does not include poloidal mode number information. The resulting field amplitudes are $\sim 0.012\,\mathrm{G\,A^{-1}}$ of $n = 1$ B_R perturbation. This implies that the 2.5 kA $n = 1$ perturbations in figure 11 correspond to ~ 30 G of $n = 1$ applied field. When the same analysis is computed for a circle displaced to $Z = -1$ m, but still at $R = 1.45$, the resulting $n = 1$ B_R perturbation is $\sim 0.0015\,\mathrm{G\,kA^{-1}}$, corresponding to ~ 4 G of $n = 1$ perturbation. These should be compared to the 4.5 kG (at $R \sim 1$ m) TFs that are most common in NSTX experiments; the applied field magnitudes that may result in some suppression of the halo current

asymmetry rotation are between 6×10^{-3} and 10^{-4} of the applied TF.

In the specific experiments, large $n = 1$ fields were applied during deliberate VDEs. These were quite rapid VDEs, where radial field feedback was deliberately frozen [63] at $t = 0.3$ s; the plasma was then actively pushed down by applying a positive bias to the upper radial field coil and a negative bias to the lower radial field coil. The vertical motion under these scenarios begins to clearly grow at ~310 ms, with, as shown in figure 12(*a*), disruption following at ~340 ms. These scenarios produce the largest halo current fractions measured in NSTX [41]. As shown in figure 12(*b*), $n = 1$ fields of various amplitudes were applied, starting at 0.3 s. This is sufficiently late that the fields do not impact the main portion of the discharge, but sufficiently early that the fields can penetrate the vessel and passive plates by the time of large halo currents.

The results of this experiment are shown in figures 12(*c*) through (*g*). Discharges 140444 and 140452 are reference discharges with no $n = 1$ applied fields. They have quite similar VDE growth rates and disruption times. One of them (140452) shows approximately 1 revolution worth of rotation; the other (140444) shows essentially no toriodal rotation. Note that because these deliberate VDEs tend to have very large halo currents and halo current fractions [41], the data in figure 10 indicates that many toroidal revolutions should not be expected under those conditions.

Discharges 140453, 140454 and 140455 have 750 kA, 1500 kA and 1000 kA of power supply current, respectively. All three of these cases show ~1.5 total revolutions, which is comparable to that in one of the reference cases, and exceeds the number of revolutions in the other. Note that the case with 1500 kA of $n = 1$ coil current actually disrupts before contact with the divertor floor is made; it appears likely that an $n = 1$ locked mode is driven in this case. Nevertheless, tordoidal rotation of the asymmetry is observed.

The conclusions of this section are thus somewhat mixed. There is some evidence that very large $n = 1$ fields can eliminate the cases with many toroidal rotations, though the statistics behind this observation are far from conclusive. However, in VDE disruptions prone to having large halo currents and only a single toroidal revolution, the $n = 1$ applied fields had no apparent impact on the rotation dynamics.

6. Halo current symmeterization during the late current quench

As noted in the context of figures 2–6, there is a tendency for the halo current entrance point magnitude to become tordoidally symmetric during the last phase of the disruption. This section will show a likely explanation for this observation: that the symmeterization time corresponds to the time when the magnetic axis has been nearly or completely driven into the lower divertor plate, and the open-field line currents dominate.

There does not exist a code that can compute the experimentally constrained 3D or 2D force-balance equilibria during this phase of the discharge. In particular, the 2D equilibrium fitting codes used at NSTX, EFIT first described in [64] and implemented at NSTX as per [65, 66], and LRDFIT [67], have typically not been run in a way allowing current outside the separatrix. Rather, the toroidal currents are related to the pressure and current profiles as per the Grad–Shafranov equation, $J_\phi = Rp' + (\mu_0/R)ff'$, where the pressure p and $f = RB_T$ are functions of poloidal flux within the separatrix [68].

Instead, the disrupting plasma is modelled here as a group of axisymmetric filaments. This fitting procedure, part of the LRDFIT code, uses a regularization scheme in order to prevent unphysical current spatial variation; it also includes axisymmetric equivalent currents in the vacuum chamber wall. Note that the solutions so computed do not have an MHD force-balance constraint, and so should be viewed as approximations to the true evolution.

With that caveat, figure 13 illustrates five time slices during the later phases of the disruption, for the discharge already discussed in figures 2 and 4. The boundaries plotted in figure 2(*b*) indicate that this discharge ultimately limits the lower-outer divertor, and this is observed in the filament reconstruction at $t = 412.5$ ms. The plasma continues to move down, with the magnetic axis lost at $t \sim 414$ ms. The last reconstruction shows that some residual current is present, but that the magnetic surface configuration has essentially vanished. Looking back at figure 2, the halo current asymmetry has essentially vanished at $t = 413.6$. It can thus be inferred that the near or complete loss of the closed magnetic surface geometry during the VDE results in the loss of the halo asymmetry.

A similar calculation has been done for the discharge in figure 5; note that the discharge in that figure limited on the lower SPPs, and that a similar phase of nearly axisymmetric halo current was observed at the end of the disruptions. The SVD poloidal flux reconstruction is shown in figure 14, and shows closed poloidal flux contours limiting on the lower passive plate. This closed-flux configuration is essentially eliminated by $t = 481$ ms, which approximately corresponds to the time in figure 5 where the halo currents become toroidally symmetric.

7. Summary and discussion

This paper has documented a number of features of the halo current asymmetry in NSTX. These include the following.

- The halo current toroidal asymmetry is often observed to rotate toroidally, with up to eight total rotations detected in extreme cases (sections 3 and 4).
- In many cases, the dominant pattern of the halo current is a toroidally localized lobe, with full width at half maximums of 1.5–4 radians (section 3).
- The temporal dynamics of this rotation can be quite complicated, with rapid variations in both the rotation velocity and toroidal peaking (section 3).
- The cases with the largest halo currents typically have both smaller rotation speeds and fewer rotations (section 4).
- It appears that very large $n = 1$ applied fields may be able to eliminate the cases with many toroidal rotation. However, large $n = 1$ fields were not observed to change the rotation dynamics in scenarios with ~1 toroidal revolution (section 5).

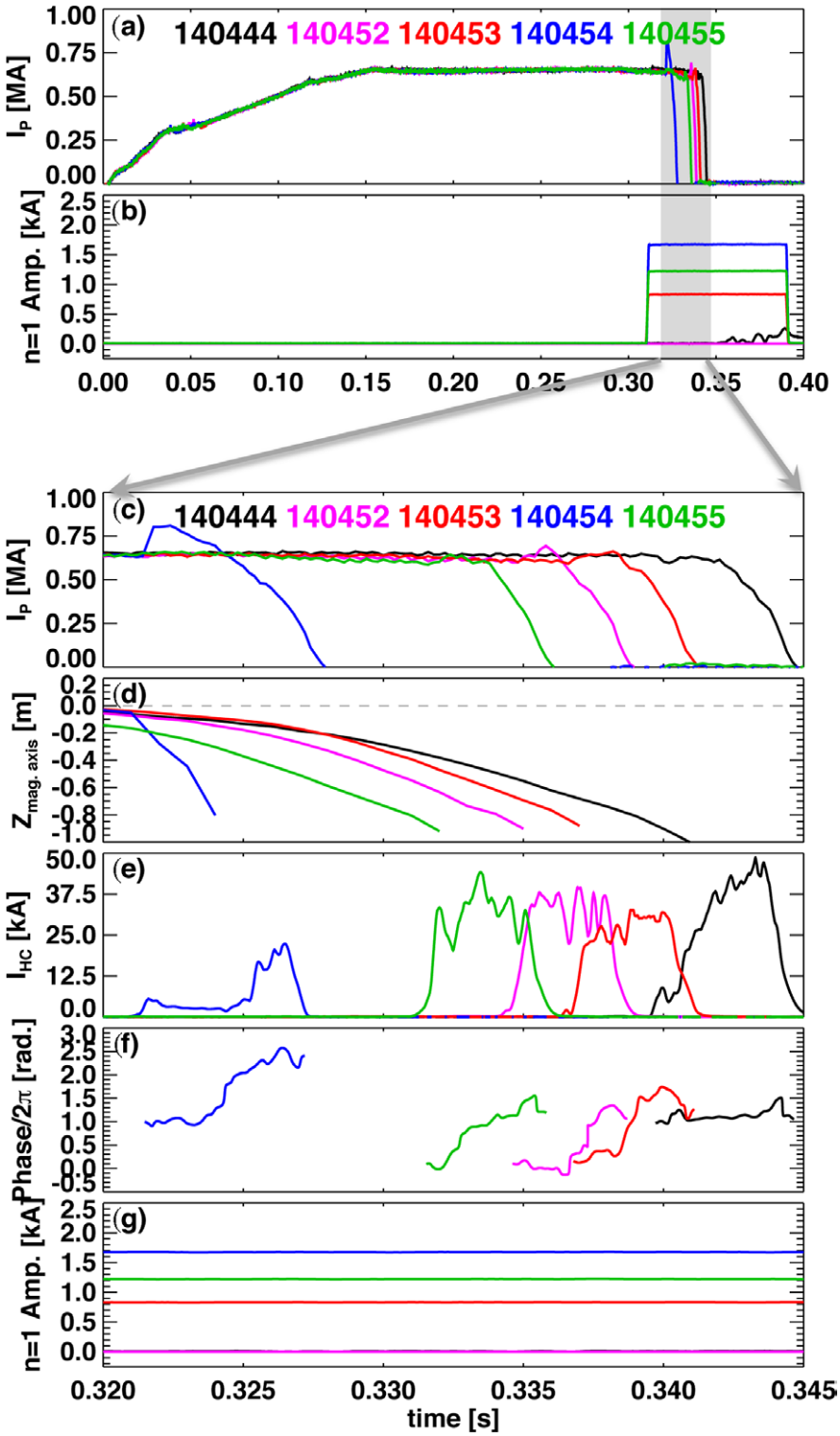

Figure 12. Plots of (*a*) the plasma current and (*b*) the applied $n = 1$ field in the upper figure, for VDE disruptions. The lower figure shows (*c*) the plasma current, (*d*) the magnetic axis location, (*e*) the $n = 0$ halo current magnitude, (*f*) the $n = 1$ asymmetry phase, and (*g*) the $n = 1$ applied field magnitude, during a small time window containing the disruption.

- The halo current asymmetry typically vanishes during the very final phase of the disruption, approximately 1 ms before the $n = 0$ halo current vanishes. This is likely due to the near or complete loss of closed-surface magnetic geometry at the end of this phase, with residual open-field line current dominating the system (section 6).

A few comments are in order to place these results in the context of the previous overview of NSTX halo currents, in [41]. Figure 7(*d*) of that paper shows a plot of the toroidal peaking factor as a function of the halo current fraction for the row-3 tiles, measured at the time of maximum halo current fraction. There is considerable scatter in that plot. In part

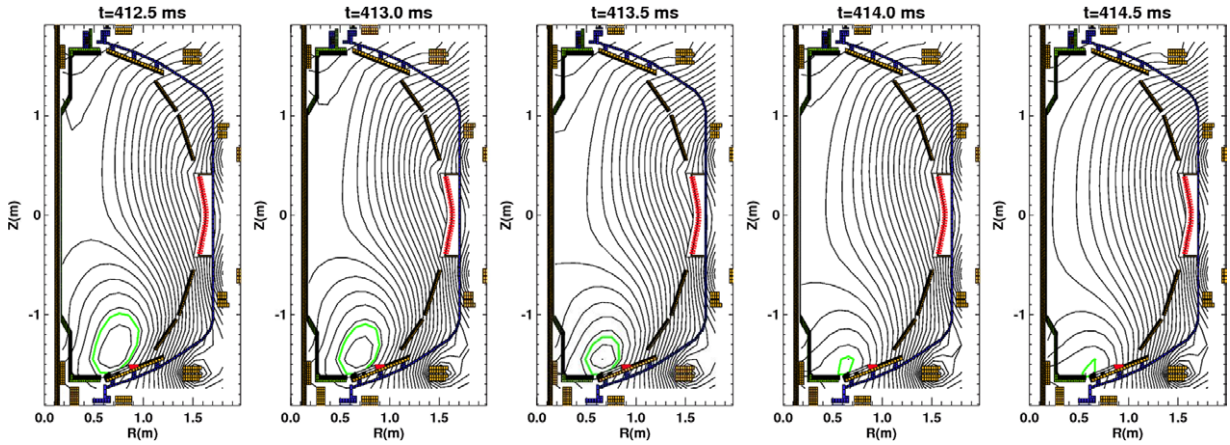

Figure 13. Evolution of the poloidal magnetic flux during the later phase of a VDE, as determined by a filament reconstruction code. The discharge in this case (141687) is the same as in figure 2.

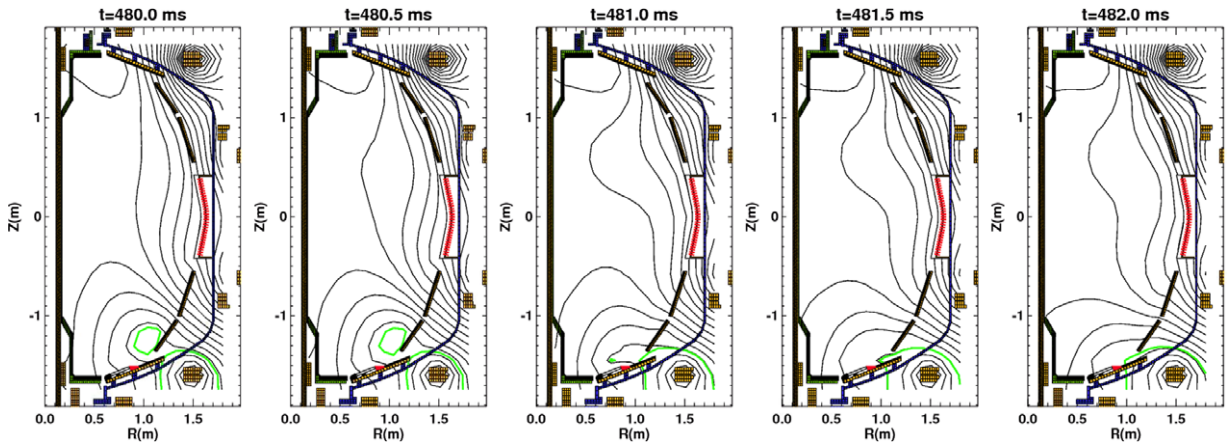

Figure 14. Evolution of the poloidal magnetic flux during the later phase of a VDE, as determined by a filament reconstruction code. The discharge in this case (139760) is the same as in figure 5.

this can be understood by looking at the TPF evolution in figures 4(*d*) and 7(*d*) of the present paper. There, it is clear that small changes in the time at which the TPF is evaluated can result in large changes in the TPF so determined. Additionally, note that the row-3 halo current fractions in that previous paper are larger than in figure 10 of the present paper, due to the fact that the present paper uses averages over different phases of the pulse, while the previous paper took the maximum halo current magnitude.

The previous paper also noted that the toroidal peaking in the chamber wall appears to be less peaked than at the entrance points. The likely explanation for this is that the currents tend to become more toroidally uniform in the large conducting structures such as the NSTX vacuum chamber. This reduction of the halo current peaking in the vacuum chamber, in particular, the centre column of a spherical torus, has been observed computationally in [69, 70].

Some of these results are potentially optimistic for future tokamak/ST reactor facilities. For instance, the observation that the largest halo currents (or halo current fractions) typically do not have many revolutions of the asymmetry is generally beneficial. The trend towards symmeterization later in the halo current phase reduces to some extent the duration of strong asymmetry. However, without a more complete understanding of the underlying rotation physics or confirmation of these trends on other, larger devices, it is difficult to extrapolate the results to future tokamaks and STs.

Acknowledgments

The author would like to thank Allen Boozer for encouragement and helpful discussion. This research was funded by the United States Department of Energy under contract DE-AC02-09CH11466.

References

[1] ITER Physics Basis Editors *et al* 1999 *Nucl. Fusion* **39** 2137
[2] Hender T.C. *et al* 2007 Progress in the ITER Physics Basis: chapter 3. MHD stability, operational limits and disruptions *Nucl. Fusion* **47** S128–202
[3] Humphreys D.A. and Whyte D.G. 2000 *Phys. Plasmas* **7** 4057
[4] Riccardo V., Barabaschi P. and Sugihara M. 2005 *Plasma Phys. Control. Fusion* **47** 117
[5] Wesley J.C. *et al* 2006 *Proc. 21st Int. Conf. on Fusion Energy 2006 (Chengdu, China, 2006)* (Vienna: IAEA) CD-ROM file IT/P1-21 and www-naweb.iaea.org/napc/physics/FEC/FEC2006/html/index.htm

[6] Gerhardt S.P., Menard J.E. and the NSTX Team 2009 *Nucl. Fusion* **49** 025005
[7] Wesley J.C. *et al* 2010 *Proc. 23rd Int. Conf. on Fusion Energy 2010 (Daejeon, South Korea, 2010)* (Vienna: IAEA) CD-ROM file ITR/P1-26 and www-naweb.iaea.org/napc/physics/FEC/FEC2010/html/index.htm
[8] Shibata Y. *et al* 2010 *Nucl. Fusion* **50** 025012
[9] Riccardo V. *et al* 2002 *Plasma Phys. Control. Fusion* **44** 905
[10] Riccardo V., Loarte A. and the JET EFDE Contributors 2005 *Nucl. Fusion* **45** 1427
[11] Sugihara M. *et al* 2007 *Nucl. Fusion* **47** 337
[12] Arnoux G., Loarte A., Riccardo V., Fundamenski W., Huber A. and JET-EFDA Contributors 2008 *Nucl. Fusion* **49** 085038
[13] Riccardo V. *et al* 2010 *Plasma Phys. Control. Fusion* **52** 024018
[14] Rosenbluth M.N. and Putvinski S.V. 1997 *Nucl. Fusion* **37** 1355
[15] Yoshino R., Tokuda S. and Kawano Y. 1999 *Nucl. Fusion* **39** 151
[16] Yoshino R. and Tokuda S. 2000 *Nucl. Fusion* **40** 1293
[17] Gill R.D. *et al* 2002 *Nucl. Fusion* **42** 1039
[18] Tamai H. *et al* 2002 *Nucl. Fusion* **42** 290
[19] Plyusnin V.V. *et al* 2006 *Nucl. Fusion* **46** 277
[20] Forster M. *et al* 2011 *Nucl. Fusion* **51** 043003
[21] Hollmann E.M. *et al* 2011 *Nucl. Fusion* **51** 103026
[22] Eidietis N.W. *et al* 2012 *Phys. Plasmas* **19** 016109
[23] James A.N. *et al* 2011 *Nucl. Fusion* **51** 103026
[24] Sizyuk V. and Hassanein A. 2009 *Nucl. Fusion* **49** 095003
[25] Schaffer M.J. and Leikund B.J. 1991 *Nucl. Fusion* **31** 1750
[26] Strait E.J. *et al* 1991 *Nucl. Fusion* **31** 527
[27] Humphreys D.A. and Kellman A.G. 1999 *Phys. Plasmas* **6** 2742
[28] Eidietis N.W. and Humphreys D.A. 2011 *Nucl. Fusion* **51** 083034
[29] Andrew P., Noll P. and Riccardo V. 1997 *Proc. 17th IEEE/NPSS Symp. on Fusion Engineering (San Diego, CA, 6–10 October 1997)* p 108
[30] Riccardo V. *et al* 2003 *Fusion Eng. Des.* **66–68** 919
[31] Riccardo V. and JET EFDA Contributors 2003 *Plasma Phys. Control. Fusion* **45** A269
[32] Riccardo V. *et al* 2004 *Plasma Phys. Control. Fusion* **46** 925
[33] Riccardo V. *et al* 2009 *Nucl. Fusion* **49** 055012
[34] Hender T.C. *et al* 2010 *Proc. 23rd Int. Conf. on Fusion Energy 2010 (Daejeon, South Korea, 2010)* (Vienna: IAEA) CD-ROM file EX/10-3 and www-naweb.iaea.org/napc/physics/FEC/FEC2010/html/index.htm
[35] Pautasso G. and Gruber O. 2003 *Fusion Sci. Technol.* **44** 716
[36] Pautasso G. *et al* 2011 *Nucl. Fusion* **51** 1
[37] Knight P.J. *et al* 2000 *Nucl. Fusion* **40** 325
[38] Neyatani Y. *et al* 1999 *Nucl. Fusion* **39** 559
[39] Granetz R.S. *et al* 1996 *Nucl. Fusion* **36** 545
[40] Counsell G.F., Martin R., Pinfold T., Taylor D. and the MAST Team 2007 *Plasma Phys. Control. Fusion* **49** 435
[41] Gerhardt S.P. *et al* 2012 *Nucl. Fusion* **52** 063005
[42] Zakharov L.E. 2008 *Phys. Plasmas* **15** 062507
[43] Zakharov L.E. 2011 *Phys. Plasmas* **18** 062503
[44] Boozer A.H. 2012 *Phys. Plasmas* **19** 058101
[45] Boozer A.H. 2012 *Phys. Plasmas* **19** 052508
[46] Manickam J., Boozer A. and Gerhardt S. 2012 *Phys. Plasmas* **19** 082103
[47] Ono M. *et al* 2000 *Nucl. Fusion* **40** 557
[48] Stevenson T. *et al* 2002 A neutral beam injector upgrade for NSTX *PPPL Report* 3651
[49] Wilson J.R. *et al* 2003 *Phys. Plasmas* **10** 1733
[50] Gerhardt S.P. *et al* 2011 *Rev. Sci. Instrum.* **82** 103502
[51] Kugel H.W. *et al* 2009 *Fusion Eng. Des.* **84** 1125
[52] Markwardt C.B. 2008 Non-linear least squares fitting in IDL with MPFIT *Proc. Astronomical Data Analysis Software and Systems XVIII (Quebec, Canada, 17 January 2013)* (*ASP Conference Series* vol. 411) ed. D. Bohlender *et al* (San Francisco, CA: Astronomical Society of the Pacific) pp 251–4
[53] Fitzpatrick R. 1993 *Nucl. Fusion* **33** 1049
[54] Shaing K.C. 1983 *Phys. Fluids* **26** 3315
[55] Shaing K.C. 2003 *Phys. Plasmas* **10** 1443
[56] Park J.-K. *et al* 2009 *Phys. Rev. Lett* **102** 065002
[57] Sontag A. *et al* 2007 *Nucl. Fusion* **47** 1005
[58] Zhu W. *et al* 2006 *Phys. Rev. Lett* **96** 225002
[59] Sabbagh S.A. *et al* 2010 *Nucl. Fusion* **50** 025020
[60] Menard J.E. *et al* 2010 *Nucl. Fusion* **50** 045008
[61] Gerhardt S.P. *et al* 2010 *Plasma Phys. Control. Fusion* **52** 104003
[62] Sabbagh S.A. *et al* 2006 *Phys. Rev. Lett.* **97** 045004
[63] Humphreys D.A. *et al* 2009 *Nucl. Fusion* **49** 115003
[64] Lao L.L. *et al* 1985 *Nucl. Fusion* **25** 1421
[65] Sabbagh S.A. *et al* 2001 *Nucl. Fusion* **41** 1601
[66] Sabbagh S.A. *et al* 2006 *Nucl. Fusion* **46** 635
[67] Menard J.E. *et al* 2006 *Phys. Rev. Lett* **97** 095002
[68] Wesson J. 1997 *Tokamaks* (Oxford: Clarendon)
[69] Pomphrey N., Bialek J.M. and Park W. 1998 *Nucl. Fusion* **38** 449
[70] Menard J.E. *et al* 2012 *Nucl. Fusion* **52** 083015